An automated framework for long-range acoustic positioning of autonomous underwater vehicles

Cristian Graupe, Lora J. Van Uffelen, Peter F. Worcester, et al.

ARTICLES YOU MAY BE INTERESTED IN

An automated framework for long-range acoustic positioning of autonomous underwater vehicles

Cristian Graupe,[1,a)] Lora J. Van Uffelen,[1] Peter F. Worcester,[2] Matthew A. Dzieciuch,[2] and Bruce M. Howe[3]

[1]*Department of Ocean Engineering, University of Rhode Island, Narragansett, Rhode Island 02882, USA*

[2]*Scripps Institution of Oceanography, University of California San Diego, La Jolla, California 92093, USA*

[3]*Department of Ocean and Resources Engineering, University of Hawaii, Honolulu, Hawaii 96822, USA*

ABSTRACT:

An automated method was developed to align underwater acoustic receptions at various depths and ranges to a single reference prediction of long range acoustic arrival structure as it evolves with range in order to determine source-receiver range. Acoustic receptions collected by four autonomous underwater vehicles deployed in the Philippine Sea as part of an ocean acoustic propagation experiment were used to demonstrate the method. The arrivals were measured in the upper 1000 m of the ocean at ranges up to 700 km from five moored, low frequency broadband acoustic tomography sources. Acoustic arrival time structure for pulse compressed signals at long ranges is relatively stable, yet real ocean variability presents challenges in acoustic arrival matching. The automated method takes advantage of simple projections of the measured structure onto the model space that represents all possible pairings of measured peaks to predicted eigenrays and minimizes the average travel-time offset across selected pairings. Compared to ranging results obtained by manual acoustic arrival matching, 93% of the automatically-obtained range estimates were within 75 m of the manually-obtained range estimates. Least squares residuals from positioning estimates using the automatically-obtained ranges with a fault detection scheme were 55 m root-mean-square.
© 2022 Acoustical Society of America. https://doi.org/10.1121/10.0013830

I. INTRODUCTION

Autonomous underwater vehicles (AUVs) have significant potential for use as long range receivers or observers in ocean acoustic experiments. These platforms are of particular interest for increasing the spatial resolution of measurements of acoustic arrival time structure during moored tomography experiments. This concept has been demonstrated with the Moving Ship Tomography Experiment (AMODE-MST Group, 1994), and AUVs could augment or replace ships as mobile receivers. The uncertainty of the platform's underwater location makes this challenging, but the acoustic signals transmitted by moored tomography transceiver arrays can be used to improve the estimated position using acoustic arrival matching (Van Uffelen *et al.*, 2016; Van Uffelen *et al.*, 2013). Acoustic arrival matching involves a "gross alignment" that determines source-receiver range for sparse, long-range measurements of acoustic arrivals by aligning the measurements to a reference prediction of the multipath acoustic arrival structure. The arrival matching is a tedious and time consuming manual process. To move towards real-time positioning of underwater platforms at long ranges using acoustics, this paper describes an automated algorithm to perform acoustic arrival matching. The automated framework accomplishes gross alignment to determine source-receiver range and additionally assigns individual peak arrivals to predicted eigenrays.

Low frequency acoustics has been used to localize underwater platforms at long ranges for the purposes of studying ocean properties with low positional uncertainty using a variety of acoustic signals and processing techniques, including Long Baseline (LBL) and long-range RAFOS systems. In particular, the RAFOS system, named as a reverse acronym for sound fixing and ranging (SOFAR), has employed narrowband linear frequency modulated (LFM) signals to track passive current-following floats for decades at ranges exceeding 1800 km in temperate ocean regions, yielding uncertainties of 1.5 to 4.5 km at these long ranges (Duda *et al.*, 2006). Experiments in long-range acoustic propagation and tomography employ sources with increased bandwidth, yielding higher temporal resolution of the received signal such that the individual travel-times associated with multi-path arrivals can be resolved (Munk *et al.*, 1995). LFM signals with wider bandwidth and lower center frequency produce a higher signal-to-noise ratio for individual detected peaks in the pulse-compressed received signal, which is beneficial to the task of resolving the acoustic arrivals (Duda *et al.*, 2006).

Broadband (100 Hz), low frequency (250 Hz) sources were deployed in a pentagonal array as part of a deep-water

a)Electronic mail: graupec@uri.edu

acoustic propagation experiment in the Philippine Sea, hereafter referred to as the PhilSea10 experiment (Worcester *et al.*, 2013). Four Seagliders, each equipped with an Acoustic Recording System (ARS), were deployed at various positions in the vicinity of the PhilSea10 acoustic array in November 2010 and passively received long-range transmissions for a period of several months. Seagliders are buoyancy driven AUVs capable of long dives that traverse the upper 1000 m of the ocean in a saw-tooth pattern, sampling ocean properties along a programmed path between way points. These dives lasted about 6 h, on average covering 3.55 km between GPS fixes at the surface, though rarely the Seaglider could travel much further in a single dive (Van Uffelen *et al.*, 2013). Although hydrodynamic models are used to estimate vehicle position, ocean currents and variations in density affect the ability to determine their positions precisely while underwater and beyond the reach of Global Navigation Satellite System (GNSS) signals (Bennett *et al.*, 2021).

Over 2000 acoustic receptions at unique locations at ranges up to 700 km were obtained from each of the five moored low frequency sources. The vehicle positioning results reported in Van Uffelen *et al.* (2013) were obtained by manually aligning these measurements to eigenray predictions for unique source-receiver geometries accounting for the tracked movement of each source. The gross time offset between the measured reception and the eigenray prediction was attributed to error in the estimated underwater position of the AUV. The corresponding range offsets were obtained by multiplying the manually-obtained time offsets by a nominal sound speed of 1500 m/s. Positioning with ranges obtained by this acoustic arrival matching method was demonstrated to produce positions with residuals on the order of 50 m root-mean-square (rms) (Van Uffelen *et al.*, 2016).

Typical analysis of acoustic receptions at known ranges in moored tomography experiments includes tracking individual ray arrivals throughout the duration of the experiment, using techniques such as Viterbi tracking (Dzieciuch, 2014). This tracking requires the moored receiver location to be known and relatively constant such that the acoustic arrival structure does not change significantly between receptions. The four Seagliders in this experiment were in constant motion, sampling the acoustic arrival structure at unique locations and depths for each reception. This limited sampling makes it impossible to track individual eigenrays throughout the experiment, and as a result, the task of eigenray identification had to be accomplished manually for each individual acoustic reception.

Ocean models constrained by measurements of sea surface height, surface temperature, and Argo observations in the North Pacific are becoming increasingly realistic. The inclusion of acoustic travel-time data from the transceiver array provides important integral constraints for a regional ocean model of the North Pacific, allowing for further corrections of the ocean interior (Gopalakrishnan *et al.*, 2021). The acoustic receptions from the four Seagliders could, in principle, provide additional integral constraints for the ocean model at an increased spatial resolution (AMODE-MST Group, 1994). To work towards using mobile receivers in acoustic tomography experiments in order to further constrain ocean models with acoustic travel-time data, the task of fully resolving individual eigenrays and computing associated travel-time offsets from the measured receptions must also be automated.

The variability of ocean sound speed in depth, range, and time is the primary source of uncertainty in the task of predicting arrival structure and associating measured peaks with eigenrays, and consequently, the measured ray arrival structure can differ from predictions in ways that make generalized automated processing difficult. The presence of internal waves, for example, can scatter acoustic energy and alter the depths of the caustics (Van Uffelen *et al.*, 2009). The scattered acoustic energy manifests itself as spurious peaks in the measured arrivals that do not appear in range independent predictions. The Philippine Sea is an area where several different water masses interact, and as a result the acoustic environment can be complicated. In addition to random internal waves, there are also internal tides, mesoscale eddies, and spicy thermohaline structure (Dzieciuch *et al.*, 2004) that all had significant impacts on the sound-speed field during the experiment (Colosi *et al.*, 2013).

In a report published in 2011 by the National Research Council's Committee on an Ocean Infrastructure Strategy for U.S Ocean Research in 2030, the need for a permanent large scale positional network for improved undersea navigation was identified (National Research Council, 2011). Multiple simple approaches were investigated by Wu *et al.* (2019) to determine acoustic ranges and ray identities by comparing measured wave forms collected during the PhilSea10 experiment and synthetic wave forms from a model of mode propagation that provides an estimate of acoustic intensity for the arrival pattern. A "cold start" solution was developed by Mikhalevsky *et al.* (2020) that achieved low position errors using the data from the fixed moorings of the PhilSea10 experiment that requires no *a priori* sound-speed information or acoustic propagation modeling, instead relying on high precision travel-time measurements of the slowest path/mode energy in the finale of the arrival pattern to simultaneously solve for a representative sound speed and a position estimate through a process of least squares inversion.

The method proposed here automates the determination of range and ray identities using the arrival structure and travel-times of the arrivals in each reception by comparing to ray predictions computed using a single range-independent sound-speed profile and a nominal source depth. In consideration of real time processing of long-range arrival-time measurements on mobile platforms, the measured acoustic arrivals are compared to a single reference prediction of the arrival-time structure as it evolves with a range from the source. The ray identity and individual travel-time errors can then be determined for each arrival. These considerations also require that the method be relatively simple, as the computational ability and working computational memory of such platforms can be limited. Here, a generalized method for aligning the measured

acoustic arrivals with predictions of the acoustic arrival structure, referred to as a Depth, Acoustic Range, reduced travel Time (DART) prediction, is presented. The objective of the method is to determine the range of the platform from the transmitting source independently for each measured reception and in the process to associate the received arrival peaks with predicted eigenray paths.

Section II outlines the data collection and processing of the raw acoustic signals, describes the reference DART prediction of the acoustic arrival structure and outlines the algorithm for automated acoustic arrival matching with ray identification that was developed. Section III compares the acoustic ranging and positioning results with the manual ranging and positioning reported in Van Uffelen *et al.* (2016). Section IV discusses the timing, computational considerations, and potential impact of these results for real-time processing. Concluding remarks are given in Sec. V.

II. METHODS

A. Data collection and processing

Acoustic travel-times along refracted-refracted and surface-reflected ray paths were measured by AUVs at many unique depths and ranges during the Philsea10 experiment (Worcester *et al.*, 2013). Four Seagliders recorded long-range transmissions of LFM tomography signals within a pentagonal array of sources from November 2010 to April 2011. The array spanned an area with a radius of approximately 330 km, and transmissions were recorded at ranges up to 700 km and depths down to 1000 m. The sources were moored at a nominal depth of 1050 m and transmitted LFM signals at 9 min intervals, cycling every 3 h beginning at 0000, 0300, 0600,...,2100 Coordinated Universal Time (UTC) every other day throughout the duration of the experiment. The gliders recorded at a 4000 Hz sample rate for 3200 s beginning at the start time of each sequence of

transmissions. In total, 2111 receptions were recorded across the four vehicles (Van Uffelen *et al.*, 2016).

The acoustic recordings obtained by each Seaglider were processed using the estimator-correlator, producing smoothed arrival patterns compared to those resulting from matched filter processing (Dzieciuch, 2014). The Seaglider, as a buoyancy driven mobile platform, shifts its center of mass and adjusts its volume to maneuver. These events, as well as other functions exercised by the AUV, can produce transient self-noise that contaminates the recordings (Ross and Van Uffelen, 2021). The broadband, impulsive noise associated with these events was removed from the raw acoustic data to mitigate the effects of glider self-noise on the pulse compression. Corrections for clock drift, source delays, and processing delays were applied to the measured travel times (Van Uffelen *et al.*, 2013). To validate the ranging results from this work, the range offsets determined by manual alignment serve as the "ground truth" alignments for each reception (Van Uffelen *et al.*, 2016).

B. Reference prediction of acoustic arrival structure

Predictions of acoustic arrival structure were computed for depths up to 5500 m and ranges up to 700 km using ZRAY, an adaptation of the ocean acoustic ray tracing software RAY (Bowlin *et al.*, 1992). A single, representative sound-speed profile based on measurements made during the PhilSea10 experiment was used for the predictions (Van Uffelen *et al.*, 2013). The source depth for the predictions, z_0, was 1059 m which coincided with the depth of the minimum sound-speed of $c_0 = 1482$ m/s (Fig. 1, left) and was the approximate depth of the acoustic sources used in the PhilSea10 experiment. Ray paths were computed for launch angles from $-17°$ to $17°$, spaced $0.01°$ apart. For each ray, the travel time τ was reduced by subtracting out a nominal travel time proportional to the horizontal range r, referenced to c_0 [Eq. (1)]. Reducing the travel times with the minimum sound speed approximately centers the slowest
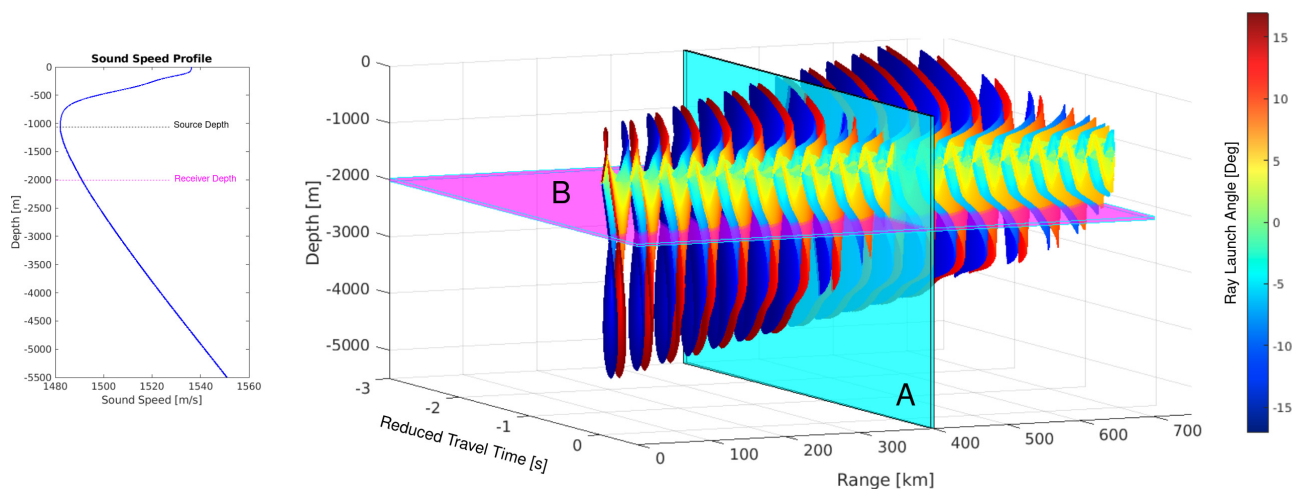
FIG. 1. (Color online) Sound-speed profile used to compute the range independent DART prediction (left) and DART prediction (right). Ray launch angles are shown on the color axis. Cross-sections of the DART prediction are shown to exemplify the full depth time front at 400 km range (A) and the eigenray progression curves at 2000 m depth (B). The cross-sections A and B correspond to the respectively marked panels in Fig. 2.

J. Acoust. Soc. Am. **152** (3), September 2022

Graupe *et al.* 1617

ducted arrivals at any given range around zero on the reduced time axis,

$$\tau_{red}(r,z) = \tau(r,z) - \frac{r}{c_0}. \qquad (1)$$

The reduced travel-time domain is convenient to evaluate potential alignments between measurements and the prediction. This adapted ray model, hereafter referred to as the DART prediction, can be evaluated at specific receiver locations to compute predicted eigenray travel times or along planes of range or depth to determine the time progression of the acoustic arrival structure (Fig. 1). A vertical slice of the DART prediction at a fixed range is an acoustic time front with a reduced time axis [Fig. 2(A)]. A horizontal slice at a fixed depth provides the range progression of the acoustical arrival time structure [Fig. 2(B)]. Unique eigenray branches, identified using the number of turning points along the ray path and the sign of the ray launch angle, can be resolved from the horizontal slice. The ray identifiers for each of these "eigenray progression curves" as they evolve with range correspond to branches on a time front (vertical slice) and vice versa (Fig. 2).

For each reception, the eigenray progression curves were interpolated over a 6000-m window centered around an initial range estimate derived from the Seaglider kinematic models, allowing up to 3000 m of range offsets in either direction. The progression curves shown in Fig. 2(B) are nearly linear within a small window of ranges, and so the curves here are linearly interpolated between eigenrays at progressive ranges with corresponding ray identifiers (Fig. 3). Although the overall structure of the time front does not change appreciably over this small range window, the change in the reduced travel time of an eigenray along individual progression curves can be significant due to range-sensitivity. The change in reduced travel time of any progression line j over the 6000 m range window is $\tau_{spread,j} = 6000 * (1/y_j)$, where y_j is the slope of the jth progression line with units m/s. The slopes computed for each eigenray progression line are nearly vertical as a result of the difference in scale between the reduced travel time and range axes (Fig. 4). For the early, higher-angle ray arrivals, the change in reduced travel time for a single progression line over a 6 km window can be as much as 0.15 s, which corresponds to an eigenray progression slope of approximately -38 km/s. The slopes of the eigenray progression curves are negative as a result of the expansion of the acoustic arrival structure with range and the method of reducing the time axis to center the slowest arrivals around zero seconds; a negative slope in the plane of reduced time and range indicates that the arrival structure is becoming more spread out in time with increased range. Because the time fronts are reduced such that the slowest arrivals are centered around zero seconds, the expansion of the arrival structure is most observable for the early arrivals and the slopes of the corresponding eigenray progression curves have a larger magnitude. The slopes computed for the early ray arrivals
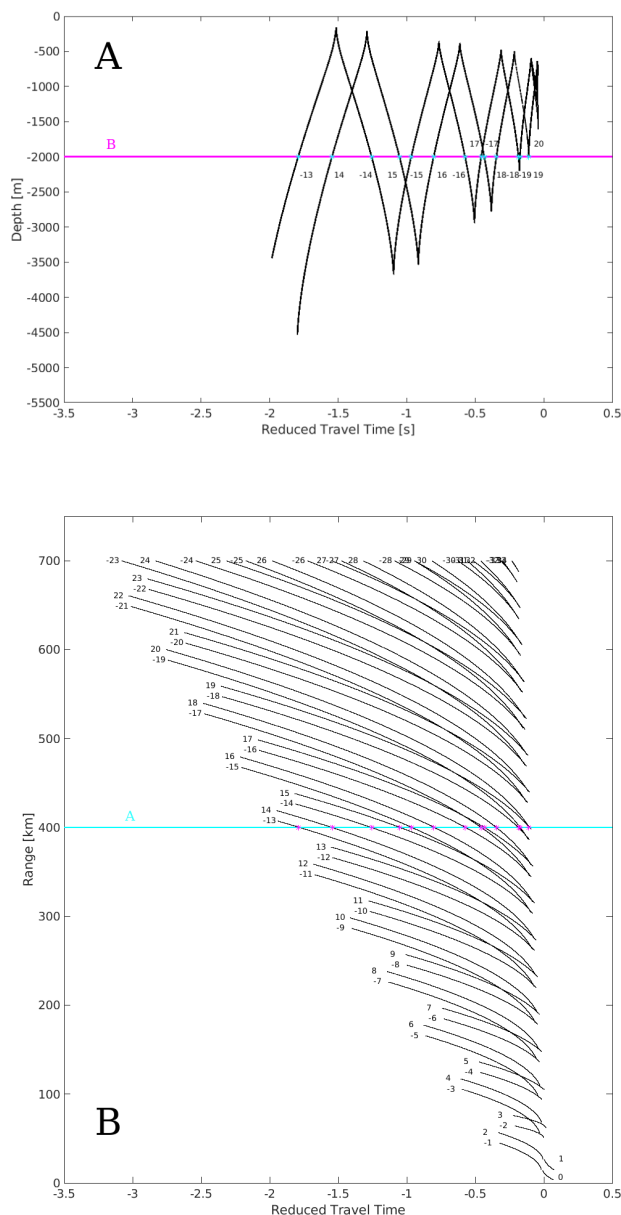

FIG. 2. (Color online) Reduced time front evaluated from the reference DART prediction at a range of 400 km corresponding to Fig. 1 (A, top). Ray identifiers are indicated for eigenrays at 2000 m. Eigenray progression curves evaluated from the reference DART prediction at a depth of 2000 m corresponding to Fig. 1 (B, bottom). The eigenrays are indicated at the receiver range of 400 km with ray identifiers. The eigenrays and ray identifiers in A and B are equivalent.

were found to be relatively constant for all ranges at a given depth except for short ranges where refractive effects have yet to become significant. For the low-angle ray paths near the finale as shown in Fig. 2(B), $\tau_{spread} \to 0$ as $(1/y) \to 0$, i.e., the DART eigenray progression lines become nearly vertical. (The eigenray progression line would be precisely vertical at $\tau = 0$ for the final arrival from the axial ray path for the case with both source and receiver at the depth of the sound-channel axis.) This is also fairly consistent over the entire range axis.

To address the issue of observed arrivals resulting from the extension of lower cusps in the time front into the
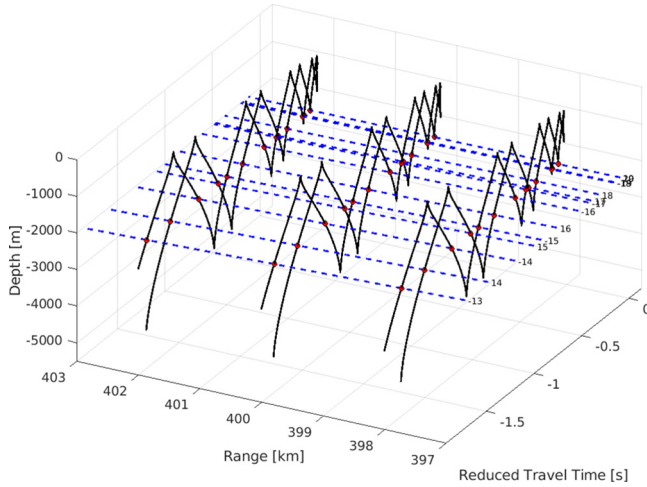
Graupe *et al.*

FIG. 3. (Color online) Reduced time fronts at ranges of 398, 400, and 402 km with linearly interpolated eigenray progression curves evaluated at a receiver depth of 2000 m indicated with dotted lines. The eigenrays and ray identities correspond to the example in Fig. 2.

shadow zone due to scattering from internal waves (Van Uffelen *et al.*, 2009), the turning points of the time fronts used to compute the eigenray progression curves were extended in depth. If there was a cusp (caustic) within 100 m of a receiver located in the shadow zone of the caustic, the caustic was extended with a straight vertical line to the receiver depth so that the reduced travel-time of the caustic was included as an 'extra' predicted arrival that would otherwise not be included in the range-independent eigenray calculations.

C. Data-eigenray pairing framework

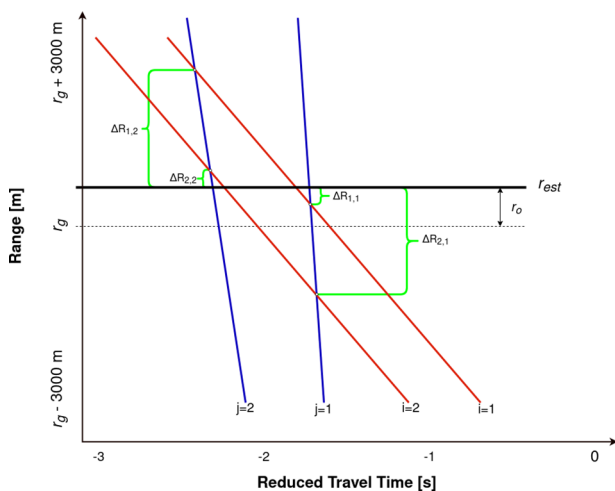In order to compare the measured arrival times to the DART prediction, the absolute travel time for any arrival i

FIG. 4. (Color online) Demonstration of intersections between projected measurements in reduced travel-time (red, denoted by i) and DART eigenray progression lines (blue, denoted by j) evaluated at the receiver depth over a 6 km range window around an initial range estimate, r_g. The range error, $\Delta R_{i,j}$, is computed relative to the initial range estimate for each intersection.

was reduced as a function of range using Eq. (2), where r_g is the initial range estimate derived from the glider hydrodynamic model and $\vec{r}$ is vector of anticipated range offsets between -3000 and 3000 m,

$$\tau_{\vec{red},i} = \tau_i - \frac{r_g + \vec{r}}{c_0}. \tag{2}$$

This is similar to Eq. (1) and projects the measured absolute arrival time onto the plane of range and reduced travel-time in the model space. On this plane, the projections intersect with the eigenray progression curves from the DART predictions (Fig. 4). Each of these intersections is a potential pairing of the ith measured arrival to the jth predicted eigenray. Aggregating information from the predictions and measurements for each pairing provides matrices of range values, reduced travel times, relative amplitude, ray identities, eigenray progression slopes, etc., that characterize potential alignments between prediction and measurement.

The alignment method described here takes advantage of the matrix of range values, **R**, for pairings between the eigenray progression curves and reduced-time measured arrival projection lines within the 6 km search window. For any given pairing of a measured arrival projection line i with a predicted eigenray progression line j, the range and travel-time errors for an arbitrary range estimate, r_{est}, can be computed from the geometry in the plane of reduced travel-time and range (Fig. 4). The range error for any such pairing is simply $\Delta R_{i,j} = R_{i,j} - r_{est}$ and the corresponding travel-time offsets between each pair of measured peaks and predicted eigenrays is computed with Eq. (3),

$$\Delta t_{i,j} = \Delta R_{i,j} \left(\frac{1}{c_0} - \frac{1}{y_j} \right). \tag{3}$$

P is defined as a vector containing selected values of N unique entries of **R** that represents a potential solution for pairing the measured arrivals to the predictions. For the example shown in Fig. 4, **R** is a 2×2 matrix and the vector $P = [R_{1,1}, R_{2,2}]$ provides the best solution. A new range estimate is defined as the mean of the values in P, i.e., $r_{est} = \bar{P}$.

The best combination of pairings will minimize the overall average squared travel-time offset among the selected pairings. The vector containing values for the corresponding travel-time offsets for each of the selected pairings in P, defined as T, can be computed with Eq. (4), where Y is the vector containing inverse values of eigenray progression slopes corresponding to each pairing. T and Y have the same length as P. For the example shown in Fig. 4, $T = [\Delta t_{1,1}, \Delta t_{2,2}]$ and $Y = [1/y_1, 1/y_2]$,

$$T = (P - \bar{P}) \left(\frac{1}{c_0} - Y \right). \tag{4}$$

The average squared travel-time offset over the combination of N pairings is given in Eq. (5). Here, the subscript "n" refers to the nth element of the vector T. Defining $r_{est} = \bar{P}$ and substituting in Eq. (3), the equation for average

squared travel-time offset for the combination of pairings becomes Eq. (6),

$$\overline{T^2} = \frac{1}{N}\sum_{n=1}^{N} T_n^2, \tag{5}$$

$$\overline{T^2} = \frac{1}{N}\sum_{n=1}^{N} \frac{(P_n - \bar{P})^2}{c_0^2} - \frac{2}{N}\sum_{n=1}^{N} \frac{Y_n(P_n - \bar{P})^2}{c_0}$$
$$+ \frac{1}{N}\sum_{n=1}^{N} Y_n^2(P_n - \bar{P})^2. \tag{6}$$

Each term in Eq. (6) is the average squared difference of the range values in P to the mean, scaled as related to the expansion after squaring the parenthetical terms in Eq. (4). Each of these terms are analogous to the scaled computation of the variance of P. The first term is on the order of 1×10^{-3} s^2, the second is on the order of 1×10^{-4} s^2, and the third is on the order of 1×10^{-5} s^2. Minimizing the squared difference of the values in P to the mean minimizes all three terms in Eq. (6). Therefore, the combination of pairings with the minimum average squared travel-time offset will also have the minimum variance among the range values of the selected pairings, providing a useful framework for determining the set that represents the best alignment between the measurements and predictions.

D. Data-eigenray search framework

The goal of this method is to find a representative combination of pairings in the model space with the smallest average squared travel-time offset (minimizing $\overline{T^2}$). Due to the complexity of propagation in a real ocean, there are often "extra" arrivals in the measured data that do not appear in the range-independent DART predictions or predicted arrivals that are not present in the data. Performing a global minimization of $\overline{T^2}$ is difficult given the ambiguity of the data, continuity requirements, and the number of ways to combine different pairings. The technique presented here defines a number of candidate solutions to minimize $\overline{T^2}$ and selects the "best" solution from among the candidate solutions. Each candidate solution is created by sequentially searching over the matrix of intersection range values, **R**, to combine potential pairings with similar range values within continuity constraints. The "best" solution is defined as the candidate solution with minimal variance among the selected range values, thus minimizing Eq. (6) among the candidate solutions. To avoid the computationally expensive task of searching over every possible combination of pairings, only the most viable candidate solutions are considered. Each candidate solution represents a unique combination of pairings where the most prominent measured peak is paired first to a different predicted eigenray. Thus, the number of potential combinations considered is the same as the number of columns in **R**. Each candidate P_j is developed by selecting an initial starting value within **R**, and sequentially adding additional pairings from each row of **R**, corresponding with the

measured peaks, until the combined set is complete, i.e., when no more pairings can be added to the combination within constraints (Figs. 5 and 6). Due to the complexity of the measured acoustic arrivals, it is not always the case that every measured peak will be assigned to a predicted eigenray and vice versa. Therefore, it is possible that the different candidate solutions will contain different numbers of pairings. The variance is scaled by the number of elements in each candidate solution and therefore should be comparable for candidates with varying numbers of elements. However, to mitigate cases where some combinations contain significantly fewer elements, the final comparison is only made between
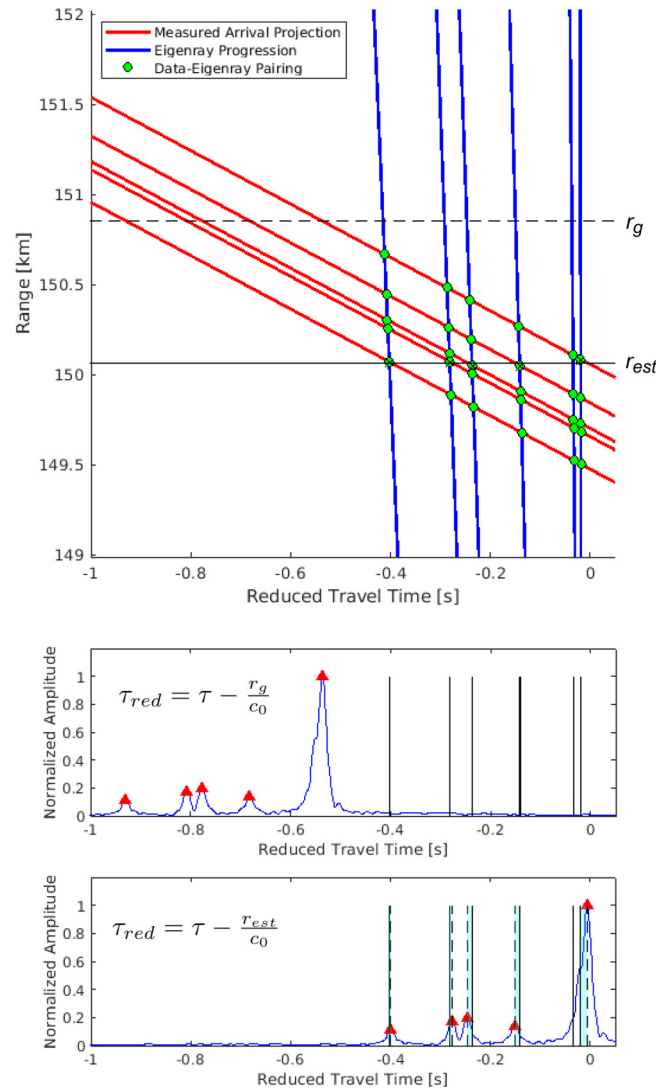
FIG. 5. (Color online) Example of the Data-Eigenray Pairing framework for an acoustic reception measured around 150 km from the source at a depth of 890 m (top). Each of the five measured arrivals were projected onto the model space where they intersected with six eigenray progression curves evaluated from the DART prediction. Measured arrival pattern in reduced travel time using the glider-derived range estimate, with peaks marked with triangles and eigenray predictions shown as vertical solid lines (Middle). Measured arrival pattern in reduced travel time aligned to eigenrays using the automatically-obtained range estimate (bottom). Resulting travel-time offsets between measured peaks and associated eigenrays are shown as a shaded area between dashed and solid lines.

1620   J. Acoust. Soc. Am. **152** (3), September 2022
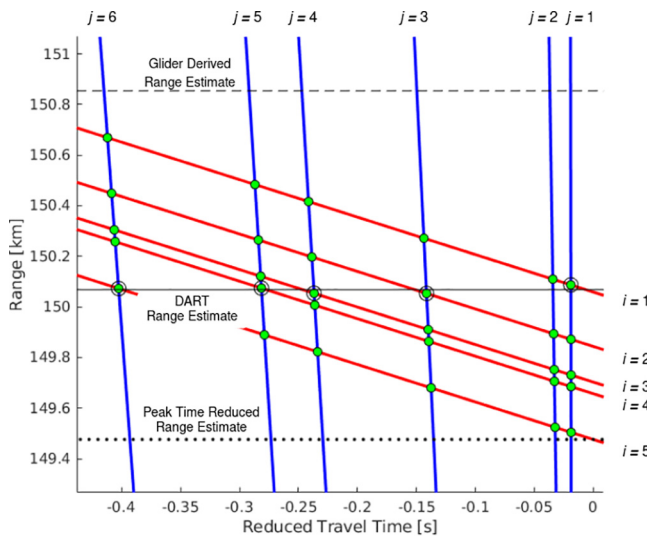
Graupe *et al.*

FIG. 6. (Color online) Example of the Data-Eigenray Pairing framework for the acoustic reception shown in Fig. 5, zoomed in to show the DART-Eigenray pairs annotated with the indices that correspond to Eq. (7). The selected pairings for the chosen combination are marked with large circles and the corresponding range estimate from the DART search method is shown with a solid horizontal line. The initial glider-derived range estimate is shown with a horizontal dashed line. An alternative initial range estimate from solving $\tau - (r_{est}/c_0) = 0$ using the absolute travel-time of the fifth measured peak is also shown.

candidate solutions that contain a relatively large number of pairings for each reception. Candidate solutions containing fewer than 75% of the maximum number of pairings among all of the candidate solutions were not considered in the final comparison. To prioritize prominent peaks in the measured data, the rows of **R** are searched in descending order of their corresponding peak prominence, beginning with the most prominent peak. Because the search is sequential, this effectively weights more prominent peaks to have a stronger influence over the final range estimate. This technique guarantees that the most prominent peak will always be assigned to a predicted eigenray and any "unmatched" peaks will likely have much lower prominence.

This section follows the example of the data-eigenray pairing shown in Figs. 5 and 6. In this example, there are five measured peak arrivals and six eigenray progression lines. Therefore, **R** is a 5×6 matrix [Eq. (7)]. In this example, the most prominent measured peak is the slowest measured arrival, which corresponds to the first row of **R**. There are six predicted eigenrays that the most prominent peak could potentially be paired with, so there six potential combinations are considered, where P_j begins with the value $R_{1,j}$,

$$
\mathbf{R} = \begin{bmatrix}
R_{1,1} & R_{1,2} & R_{1,3} & R_{1,4} & R_{1,5} & R_{1,6} \\
R_{2,1} & R_{2,2} & R_{2,3} & R_{2,4} & R_{2,5} & R_{2,6} \\
R_{3,1} & R_{3,2} & R_{3,3} & R_{3,4} & R_{3,5} & R_{3,6} \\
R_{4,1} & R_{4,2} & R_{4,3} & R_{4,4} & R_{4,5} & R_{4,6} \\
R_{5,5} & R_{5,2} & R_{5,3} & R_{5,4} & R_{5,5} & R_{5,6}
\end{bmatrix}. \tag{7}
$$

This example follows the construction of the vector P_1, which contains the range values for the combination of

pairings starting with $R_{1,1}$. At the starting point, $P_{1,0} = [R_{1,1}]$. Here, the "0" subscript is shown to denote the initial step of the iterative process and indicate that the construction of the vector is incomplete. The next pairing is from the row corresponding to the next most prominent peak. In this example, this is the third row of **R**. The "search vector" from which the next pairing is selected is comprised of the non-zero entries of the element-wise multiplication of **R** with a logical mask $\mathbf{W}_k$, where the subscript k identifies the current step of the iterative process. The logical mask is used to build in constraints for the search vector. The search is constrained so that the order of the measured peaks and predicted ray arrivals is preserved; the selection is not allowed to "cross" a pairing that has already been selected and so the selection is said to be "continuous" with respect to the down-right diagonal. This is similar to the continuity constraints in time warping algorithms such as Dynamic Time Warping (Sakoe and Chiba, 1978).

For the first step in this example, the search vector is defined by the logical mask in Eq. (8). Since there was already a selection from the first column of **R**, the indices in that column are zeroed out. The remaining indices in the third row are set to 1 and the resulting search vector is $[R_{3,2}, R_{3,3}, R_{3,4}, R_{3,5}, R_{3,6}]$. The cost function [Eq. (9)] is invoked to compute the squared travel time offsets for all of the pairings in the search vector relative to the mean of the selected values. For the first step, the starting value is $\overline{P_{1,0}} = R_{1,1}$. The pairing in the search vector with the minimum squared difference is selected and combined with the other pairings in the potential vector. In this example, the selected pairing is $\min(C_{1,1}) = R_{3,4}$. The potential vector is updated to include the selected pairing for the first step where $k = 1$, $P_{1,1} = [R_{1,1}, R_{3,4}]$. The cost function invoked at each step k uses $\overline{P_{j,k\overline{1}}}$, defined as the mean of the values in the vector at step $k-1$, as a reference for attempting to minimize the squared difference in travel time.

$$
\mathbf{W}_1 = \begin{bmatrix}
0 & 0 & 0 & 0 & 0 & 0 \\
0 & 0 & 0 & 0 & 0 & 0 \\
0 & 1 & 1 & 1 & 1 & 1 \\
0 & 0 & 0 & 0 & 0 & 0 \\
0 & 0 & 0 & 0 & 0 & 0
\end{bmatrix}, \tag{8}
$$

$$
C_{j,k} = (\mathbf{R}^{\circ}\mathbf{W}_k - \overline{P_{j,k\overline{1}}})^{\circ 2}. \tag{9}
$$

The next step is to repeat the selection process for the row corresponding to the next most prominent peak. In this example, this is now the fourth row. The logical mask is updated to define the new search vector [Eq. (10)]. Now there have been selections from both the first and third columns. Because down-right continuity must be preserved, only columns to the right of the third column can be included in the search vector. Again, the cost function is called to determine the pairing within the search vector that is nearest to $\overline{P_{1,1}}$. After this selection, the vector is updated again to include the selected pairing for step $k=2$, $P_{1,2} = [R_{1,1}, R_{3,4}, R_{4,5}]$,

J. Acoust. Soc. Am. **152** (3), September 2022

Graupe *et al.*   1621

$$\mathbf{W}_2 = \begin{bmatrix} 0 & 0 & 0 & 0 & 0 & 0 \\ 0 & 0 & 0 & 0 & 0 & 0 \\ 0 & 0 & 0 & 0 & 0 & 0 \\ 0 & 0 & 0 & 0 & 1 & 1 \\ 0 & 0 & 0 & 0 & 0 & 0 \end{bmatrix}. \qquad (10)$$

The process is repeated for the row corresponding to the next most prominent peak which is now the second row. The logical mask is updated again, now only allowing selection between the first and fourth columns as the down-right continuity dictates the selection cannot cross-the selections already made in the first and third rows [Eq. (11)]. The cost function is invoked and the vector is updated to include the new selection. This process is repeated for the remaining rows until no more selections can be made. Once the vector is complete, the mean of the range values in $P_{1,*}$ becomes the range estimate from which the travel-time offsets can be computed using Eq. (4). Here, the * subscript indicates that the construction of the vector for the potential combination is complete. The variance of the range values in $P_{1,*}$ represents the "score" for the "goodness" of the potential fit, where a lower variance corresponds to a better score,

$$\mathbf{W}_3 = \begin{bmatrix} 0 & 0 & 0 & 0 & 0 & 0 \\ 0 & 1 & 1 & 0 & 0 & 0 \\ 0 & 0 & 0 & 0 & 0 & 0 \\ 0 & 0 & 0 & 0 & 0 & 0 \\ 0 & 0 & 0 & 0 & 0 & 0 \end{bmatrix}. \qquad (11)$$

Vectors are developed for the potential combinations beginning with each of the remaining columns of **R**, each with a final range estimate, travel-time offsets, and variance to represent the goodness of fit. Finally, the potential set with the lowest variance is the set of pairings that produces a range estimate corresponding to the best fit to the eigenray predictions. In the example shown in Fig. 5, this is the potential set with starting point $R_{1,1}$, where $P_{1,*} = [R_{1,1}, R_{2,3}, R_{3,4}, R_{4,5}, R_{5,6}]$ and $r_{est} = \overline{P_{1,*}}$.

This automated pairing framework was applied to obtain range estimates and travel-time offsets/ray identities for the arrivals measured by the four Seagliders in Van Uffelen *et al.* (2016).

E. Least squares positioning

The least squares positioning process outlined for the manually-obtained ranges in Van Uffelen *et al.* (2016) was replicated for the "Conservative Doppler" case that used the initial positions derived from the Seagliders' glide slope model (GSM). In total, there were 367 reception groups containing three or more valid range estimates that allowed for trilateration. The least squares positioning process was repeated for the ranges obtained using the automated method with updated *a priori* error estimates.

The vertical glider descent and ascent velocities calculated from the pressure sensor were approximately 9 cm/s for a typical dive. The forward glider velocity was estimated to be 17 cm/s, and the average time to a GPS position fix

was about 100 min. Range uncertainty due to Doppler effects on the LFM transmissions was conservatively estimated to be (46 ms *1500 m/s)^2 = 69^2 m^2 for a glider traveling at 17 cm/s directly towards a source (Duda, 1993). Uncertainty due to ocean sound speed variability was estimated to be (70 ms *1500 m/s)^2 = 105^2 m^2 (Van Uffelen *et al.*, 2016).

Bottom-mounted transponders tracked the moored sources as they moved in response to ocean currents throughout the experiment, and the depths of the five sources varied by ±25 m on average. The horizontal positions of the moored sources were directly accounted for in the range estimation for both the manual and automated alignments. The eigenray predictions used for the manual alignment incorporated the measured source depths at the time of each transmission. The DART predictions used here were generated using a single source depth for all sources, and as a result, there is an uncertainty associated with the variation in the true source depths for the automated processing using the DART prediction. This range uncertainty was estimated to be (3 ms *1500 m/s)^2 = 4.5^2 m^2 and was rounded up to 5^2 m^2.

The range uncertainty due to manual arrival pattern matching was estimated to be (10 ms *1500 m/s)^2 = 15^2 m^2. An additional (10 ms *1500 m/s)^2 = 15^2 m^2 of uncertainty was associated with the automated arrival pattern matching, accounting for the 15 m difference between medians of the two sets of ranging results.

The least squares inversion process for positioning is sensitive to outliers; a single incorrect range estimate used in the inversion can produce residuals on the order of hundreds of meters. To mitigate the influence of outliers, a simple scheme for Fault Detection and Exclusion (FDE) was employed, similar to the way that the Global Positioning System (GPS) excludes inconsistent measurements (Zabalegui *et al.*, 2021). In the fault detection scheme, the residuals of the least square inversion are compared for each position estimate. The residuals associated with individual receptions in each position estimate are combined into the rms-residual, which is used as the test statistic for fault detection. The rms-residual is a measure of self-consistency for the ranges used in the least square inversion for a single position estimate. A fault detection threshold is defined as an upper limit for the acceptable rms-residual computed for a single position estimate. If the rms-residual is above the defined fault detection threshold, and there is redundant information available (reception groups with four or five receptions used to compute the position), the position is recomputed without the reception having the largest absolute individual residual. The least squares positioning results using the automatically-obtained ranges were compiled and compared for three cases of the FDE scheme with different detection thresholds for rms residual; 200, 150, and 100 m. The FDE scheme was only applied to reception groups where redundant information was available, so the FDE scheme does not change the total number of positions reported.

III. RESULTS

A. Automated acoustic ranging

The offsets obtained by automated alignment to the DART predictions are compared to offsets obtained by manual alignment to range-independent ray predictions as presented in Van Uffelen *et al.* (2013). In total, 1727 receptions were used in the least squares positioning process. A visual comparison of both the manual and automated alignment results shows that the structure of acoustic arrivals in reduced travel time as a function of range emerges when the measurements are aligned by the automated algorithm just as it does when they are aligned manually (Fig. 7).

Of the automatically-obtained range estimates used for vehicle positioning, 93% were within 75 m of the corresponding manually-obtained range estimates. There was no apparent trend in the agreement between the two methods with range or depth (Fig. 8). Inspection of automated alignments that differed by more than 75 m from manually-obtained ranges indicated that these receptions were often affected by high noise floors (e.g., from glider self-noise or environmental noise) or by scattering effects near predicted caustics. Overall, the automated alignments compare well to their manual counterparts. There is no degradation of performance along either spatial axis, indicating that the performance of this method is consistent over long ranges and depths spanning the upper 1000 m of the ocean.

B. Least squares positioning

The estimated uncertainties, fault detection information, and least squares inversion statistics are reported in Table I and compared with the manual results from Van Uffelen *et al.* (2016). The "Automated" and "Automated with FDE" columns report results for the same receptions and positions using the corresponding automated range estimates and fault detection thresholds. In all cases, the *a posteriori* uncertainties in x and y were comparable within a few meters of the values reported for manual ranging because they are dominated by the range uncertainty due to ocean sound-speed variability. The rms-residual of the least squares process repeated using the automated ranging estimates was 86 m, compared to 53 m for the manual results reported in Van Uffelen *et al.* (2016). This higher residual is attributed to the relatively small number of faulty automated range estimates that were included in the inversions for this case. Using a fault detection threshold of 200 m, 34 faults out of the 1727 automatically-obtained ranges were detected and excluded from the least squares inversion process. Excluding these 34 faulty receptions reduced the rms-residual from 86 to 58 m. Decreasing the fault detection threshold to 150 m further reduces the residual to 55 m. The results, in this case, are the most comparable to the results for the manual case. The majority of excluded receptions also had a high disagreement between the manual and automated range estimates (Fig. 8), suggesting that the FDE scheme with a properly set fault detection threshold could be used to evaluate the
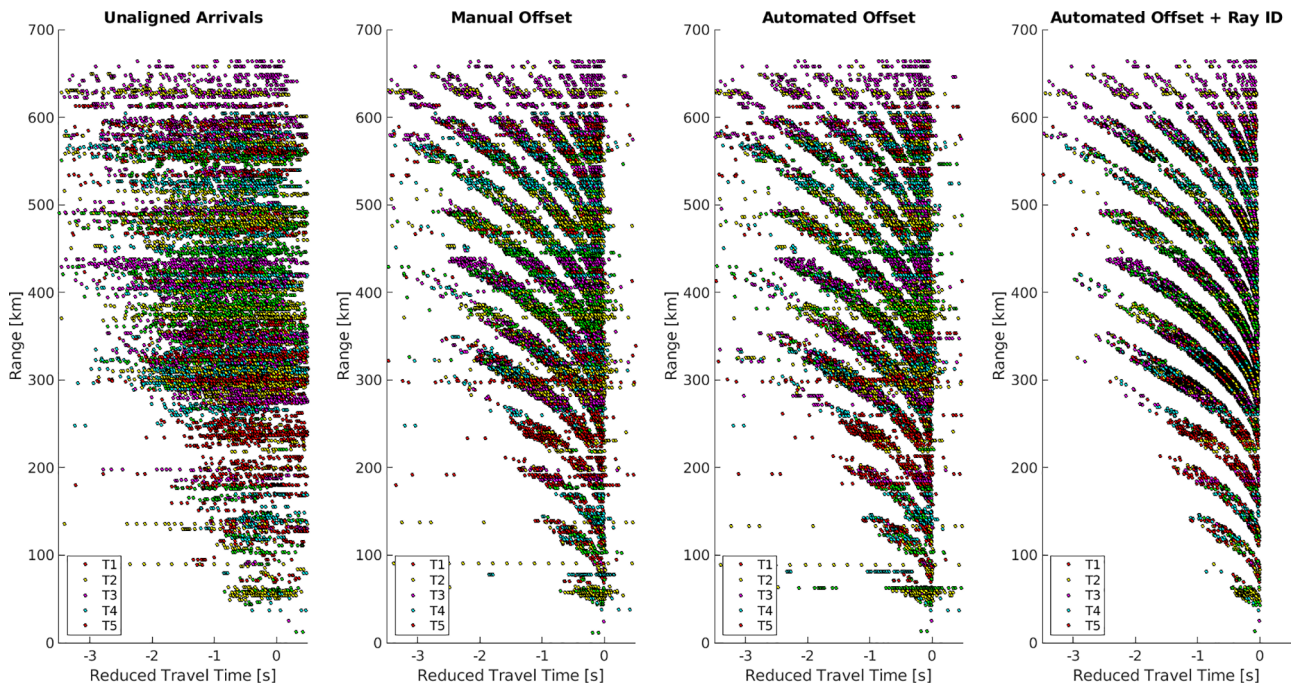

FIG. 7. (Color online) Compilation of arrival peaks for all usable receptions on the reduced time axis at ranges out to 700 km and depths down to 1000 m. The unaligned raw measured travel-times for each reception are shown with the time axis reduced using a range derived from the position estimated by the glider's hydrodynamic model (far left). The same receptions are shown with the time axis reduced using range estimates obtained by manual alignment (center-left) and range estimates obtained by the automatic alignment (center-right). In addition to the automated gross offset, the individual travel-time offsets for each measured ray arrival are applied to show the ray identification for selected peaks (far right).
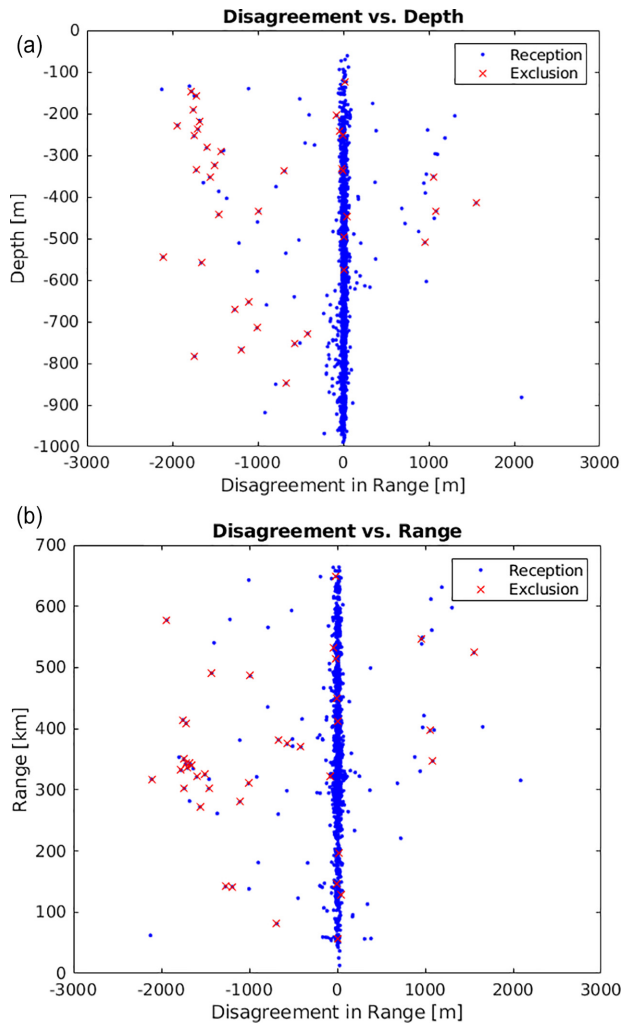
FIG. 8. (Color online) Disagreement between the manually and automatically obtained range estimates for receptions used in the least squares positioning plotted against the receiver depth (top) and the receiver range (bottom). An *x* denotes a reception that was identified as a fault using a 150 m fault detection threshold and was excluded from the positioning calculation.

TABLE I. Positioning uncertainty for the manual and automated methods of ranging with and without fault detection and exclusion (top). Fault detection thresholds and number of excluded receptions for each threshold case (middle). Least square inversion statistics for the manual and automated methods with and without fault detection and exclusion (bottom). All values given are rms values.

Data Error R	Manual	Automated	Automated with FDE		
Pattern Matching (m)	15	30	30	30	30
Sound Speed (m)	105	105	105	105	105
Doppler (m)	69	69	69	69	69
Source Depth (m)	0	5	5	5	5
Total R (m)	127	129	129	129	129
Fault Detection					
Threshold (m)	—	—	200	150	100
Number of Exclusions	0	0	34	39	63
Inversion Statistics					
a posteriori error, P_d, in x/y (m)	105/106	106/107	105/106	105/107	107/110
Residuals (m)	53	86	58	55	47

Arrival Matching process described in Van Uffelen *et al.* (2013) and Van Uffelen *et al.* (2016). These results approach the 50 m residuals for positioning uncertainty reported in Van Uffelen *et al.* (2016) while simultaneously solving for the travel-time offsets of individual peaks that could inform tomographic inversions and allow for mobile platforms to be used to increase the number of available nodes in tomography arrays as discussed in studies (Cornuelle, 1985; Duda *et al.*, 2006; Gaillard, 1985).

The generalized algorithm is constrained by the size of the search window ($+/-$ 3 km) and the maximum allowed travel-time error associated with any individual peak (0.075 s). These constraints were based on the anticipated maximum required range and travel-time offsets informed by the positioning uncertainty from the vehicle kinematic models. Although this search window is centered around the original range estimate derived from a vehicle kinematic model, the original estimate of the source-receiver range does not need to be precise. The range $r_0 = c_0 * \tau$ computed using the travel time τ of the slowest measured peak provides an initial estimate that is sufficiently close for the algorithm to compute an updated range. For the example shown in Fig. 6, the range estimate derived from the glider kinematic model is shown along with the range estimate computed using the reduced travel time of the earliest arrival. Here, the earliest arrival was selected for visibility in the figure, but the latest arrival could also be used. Regardless of which range estimate is used to center the search window, the same final range estimate is produced by the DART framework as long as the window is large enough to capture all intersections in the model space. In some cases, the window may not capture all of the intersections, but these cases are rare and can be compensated for by increasing the size of the window. In order to quantify the effect of choosing a different initial range estimate on the

consistency of automated alignments in the absence of manual alignments for direct comparison.

Decreasing the fault detection threshold to 100 m further reduces the residual to 47 m, which is below the residual reported for the manual case. However, the *a posteriori* error for this case increased by several meters, indicating that a 100 m threshold may be too constrained and may be excluding valid ranging results that should be included in the inversion. In the absence of "ground-truth" comparisons, the fault detection can be tuned by comparing the reduction in the rms of the residuals to the *a posteriori* error for different fault detection thresholds.

IV. DISCUSSION

The results presented in Figs. 7 and 8 are a compelling demonstration that the automated algorithm for alignment of received acoustic receptions with a single DART prediction is comparable to results obtained using the manual Acoustic

Graupe *et al.*

positioning uncertainty, the receptions were reprocessed using the range estimate computed from the slowest measured arrival time. The rms-residual for the automated receptions using these range estimates without fault detection is 87 m, to be compared with 86 m, which resulted from using the starting position estimate from the glider kinematic model (Table I). This minor increase results from rare cases when the search window is not large enough to capture all intersections.

For this long-range, deep-water dataset, the latest-arriving measured peak is typically within 2 s of the finale cut off. Centering this peak around zero on the reduced travel-time axis produces an initial range estimate that is anticipated to be within ($2\,s * 1482\,m/s = 2964\,m$) of the true range, which is within the 3 km window used here. The 2-s example here is conservative and in reality, the slowest peak is much closer to the finale in most cases. Even if the difference between the slowest measured peak and the true finale was more than 2 s, the uncertainty can be compensated for in the algorithm by increasing the size of the search window. The largest time spread for detected peaks in the data presented here was about 3.5 s, which indicates that the maximum search window size needed to compensate for the unknown original range in the most extreme cases would be about 5 km in either direction. This can also compensate for the differences between range estimates obtained from different kinematic models used to estimate position in real time. Therefore, all that is required here is a sufficiently accurate measurement of travel time using a signal with enough temporal resolution to distinguish individual peaks in the arrival structure. The limiting factor is then the accuracy of the clock used for acoustic data collection onboard the AUV.

In the algorithm presented here, the travel times and assigned time offsets for each intersection are interpolated from the eigenray progression curves, which are fit linearly to sequential slices of the DART prediction (Fig. 3). The "interpolation error," which is the difference between the travel times evaluated from the eigenray progression curves and the straight-forward eigenray predictions computed for the same source-receiver geometry, was measured to be on the order of $1 * 10^{-4}$ s. This is smaller than the temporal resolution of the pulse-compressed signal and is considered negligible.

The end goal of this work is to provide a streamlined system for processing and resolving long-range, deep-water acoustic receptions in real time, and so the AUV's computational abilities must be considered. This method reduces computational load by pre-calculating a single DART prediction for the anticipated sound-speed environment so that acoustic propagation predictions would not need to be computed locally or transmitted to the vehicle. The processing times here were measured on an AMD Ryzen 7 CPU (Global Foundries, Malta, NY), running on one computational core. For a typical reception, the total processing time is less than 5 s. The slowest part is the evaluation and interpolation of the time fronts. In this work, seven time fronts were interpolated over the 6 km search window (–3, –2,…, 2, 3 km), which takes about 3.5 s on average. Interpolating

the eigenray progression curves from consecutive time fronts and computing the intersection matrices only takes about 0.075 s on average. The minimum variance search is even faster, only taking about 0.015 s for typical receptions. The DART prediction used here took up 956 MB of memory, but this could be reduced. Note that the moored sources used in the PhilSea10 experiment were placed at the same nominal depth so the same DART predictions could be used for each of the 5 sources. However, the placement of the source in depth does have an impact on the predicted acoustic arrival structure. In a different experimental setup where the sources are each placed at significantly different depths, the automated acoustic arrival matching method introduced here would require different DART predictions for each source. Thus, it is desirable, with respect to the computational limitations of the AUV, to place the sources at the same depth. This approach is also applicable only within regions where the sound-speed environment is fairly range independent, as was observed in the PhilSea10 experiment. The method allows for variability in the sound-speed, such as variability associated with internal waves; however, it may not be as applicable for much larger scales or for regions that cannot be adequately characterized by a single sound speed profile.

While the ability of this method to determine the acoustic range was compared to manual alignments, the ability to resolve individual rays correctly could not be quantified directly using these observations, although the results shown in Fig. 7 are encouraging. Moreover, the data collected by the Seagliders was limited to the upper 1000 m of the ocean, so this method was not evaluated for the full ocean depth. This could be investigated using modeling including simulated data that includes time scattering statistics from Monte-Carlo-style simulations of acoustic propagation through random internal wave fields, which could also help inform the algorithm constraints. For example, the range-independent travel-time offset constraint used here (0.075 s) could be changed to better reflect the range-dependent time-scattering statistics. This simulated dataset could be used to quantify performance in regions not sampled by the Seaglider as well as quantify the ability of the algorithm to resolve both ranges and ray identities using known (simulated) offsets and travel-time errors.

Although the sequential method determines range estimates that compare well to their manually-obtained counterparts, the approach introduced here does not consider all possible combinations of the pairings defined in the framework and is not a global minimization scheme. While the complexity of the data makes true global minimization difficult, methods that utilize alternative data structures or other techniques such as machine learning might provide a more global solution.

V. CONCLUDING REMARKS

The algorithm presented here is a relatively simple and effective approach to estimating the range from the acoustic

J. Acoust. Soc. Am. **152** (3), September 2022

Graupe et al. 1625

arrival structure, showing that sparse acoustic travel-time measurements taken at many ranges and depths from multiple sources can be interpreted using a prediction of the evolution of the acoustic time front with range based on a single range-independent sound-speed profile. The automated approach directly solves for range and resolved ray identities from the acoustic arrival structure with results that are comparable to manual processing on the same data set with 93% of the automatic range estimates being within 75 m of the corresponding manual range estimates. Using the "agreement" as a metric for performance, the automated method suffered no degradation in performance at ranges out to 700 km or at depths down to 1000 m. However, scattering effects near caustics, which cause arrivals that do not appear in predictions for a range independent sound-speed profile, can sometimes cause the automated method to produce a faulty range estimate. These faulty range estimates can be mitigated during positioning using fault detection if redundant information is available. Applying the FDE scheme with a 150 m threshold to the automated case reduced the residuals to 55 m rms, compared to 53 m rms for the manual case. The *a posteriori* errors for this case were within a meter of the manual results. The combination of the automated ranging method with the simple scheme for residual-based fault detection produced positioning results comparable to the performance of the manual method, demonstrating a reliable method for automated underwater acoustic localization of submerged platforms.

ACKNOWLEDGMENTS

AMODE-MST Group (**1994**). "Moving ship tomography in the northwest Atlantic Ocean," EOS Trans. AGU **75**, 17–21.

Bennett, J. S., Stahr, F. R., Eriksen, C. C., Renken, M. C., Snyder, W. E., and Uffelen, L. J. V. (**2021**). "Assessing Seaglider model-based position accuracy on an acoustic tracking range," J. Atmos. Oceanic Technol. **38**(6), 1111–1123.

Bowlin, J. B., Spiesberger, J. L., Duda, T. F., and Frietag, L. F. (**1992**). "Ocean acoustical ray-tracing software ray," Woods Hole Oceanographic Technical Report No. WHOI-93-10.

Colosi, J. A., Van Uffelen, L. J., Cornuelle, B. D., Dzieciuch, M. A., Worcester, P. F., Dushaw, B. D., and Ramp, S. R. (**2013**). "Observations of sound-speed fluctuations in the Western Philippine Sea in the spring of 2009," J. Acoust. Soc. Am. **134**(4), 3185–3200.

Cornuelle, B. D. (**1985**). "Simulations of acoustic tomography array performance with untracked or drifting sources and receivers," J. Geophys. Res. **90**(C5), 9079–9088, https://doi.org/10.1029/JC090iC05p09079.

Duda, T. (**1993**). "Analysis of finite-duration wide-band frequency sweep signals for ocean tomography," IEEE J. Oceanic Eng. **18**(2), pp. 87–94.

Duda, T. F., Morozov, A. K., Howe, B. M., Brown, M. G., Speer, K., Lazarevich, P., Worcester, P. F., and Cornuelle, B. D. (**2006**). "Evaluation of a long-range joint acoustic navigation / thermometry system," in *Proceedings of Oceans 2006*, September 18–21, Singapore, pp. 1–6.

Dzieciuch, M., Munk, W., and Rudnick, D. L. (**2004**). "Propagation of sound through a spicy ocean, the SOFAR overture," J. Acoust. Soc. Am. **116**(3), 1447–1462.

Dzieciuch, M. A. (**2014**). "Signal processing and tracking of arrivals in ocean acoustic tomography," J. Acoust. Soc. Am. **136**(5), 2512–2522.

Gaillard, F. (**1985**). "Ocean acoustic tomography with moving sources or receivers," J. Geophys. Res. **90**(C6), 11891–11898, https://doi.org/10.1029/JC090iC06p11891.

Gopalakrishnan, G., Cornuelle, B. D., Mazloff, M. R., Worcester, P. F., and Dzieciuch, M. A. (**2021**). "State estimates and forecasts of the Northern Philippine Sea circulation including ocean acoustic travel times," J. Atmos. Oceanic Technol. **38**(11), 1913–1933.

Mikhalevsky, P. N., Sperry, B. J., Woolfe, K. F., Dzieciuch, M. A., and Worcester, P. F. (**2020**). "Deep ocean long range underwater navigation," J. Acoust. Soc. Am. **147**(4), 2365–2382.

Munk, W., Worcester, P., and Wunsch, C. (**1995**). *Cambridge Monographs on Mechanics Ocean Acoustic Tomography* (Cambridge University Press, Cambridge, UK).

National Research Council (**2011**). *Critical Infrastructure for Ocean Research and Societal Needs in 2030* (The National Academies Press, Washington, DC).

Ross, M., and Van Uffelen, L. (**2021**). "Characterizing the self-noise of a Seaglider AUV using a passive acoustic monitor," in *Proceedings of OCEANS 2021, San Diego - Porto*, September 20–23, San Diego, CA, pp. 1–5.

Sakoe, H., and Chiba, S. (**1978**). "Dynamic programming algorithm optimization for spoken word recognition," IEEE Trans. Acoust. Speech Signal Process. **26**(1), 43–49.

Van Uffelen, L. J., Howe, B. M., Nosal, E.-M., Carter, G. S., Worcester, P. F., and Dzieciuch, M. A. (**2016**). "Localization and subsurface position error estimation of gliders using broadband acoustic signals at long range," IEEE J. Oceanic Eng. **41**(3), 501–508.

Van Uffelen, L. J., Nosal, E.-M., Howe, B. M., Carter, G. S., Worcester, P. F., Dzieciuch, M. A., Heaney, K. D., Campbell, R. L., and Cross, P. S. (**2013**). "Estimating uncertainty in subsurface glider position using transmissions from fixed acoustic tomography sources," J. Acoust. Soc. Am. **134**(4), 3260–3271.

Van Uffelen, L. J., Worcester, P. F., Dzieciuch, M. A., and Rudnick, D. L. (**2009**). "The vertical structure of shadow-zone arrivals at long range in the ocean," J. Acoust. Soc. Am. **125**(6), 3569–3588.

Worcester, P. F., Dzieciuch, M. A., Mercer, J. A., Andrew, R. K., Dushaw, B. D., Baggeroer, A. B., Heaney, K. D., D'Spain, G. L., Colosi, J. A., Stephen, R. A., Kemp, J. N., Howe, B. M., Van Uffelen, L. J., and Wage, K. E. (**2013**). "The North Pacific Acoustic Laboratory deep-water acoustic propagation experiments in the Philippine Sea," J. Acoust. Soc. Am. **134**(4), 3359–3375.

Wu, M., Barmin, M. P., Andrew, R. K., Weichman, P. B., White, A. W., Lavely, E. M., Dzieciuch, M. A., Mercer, J. A., Worcester, P. F., and Ritzwoller, M. H. (**2019**). "Deep water acoustic range estimation based on an ocean general circulation model: Application to Philsea10 data," J. Acoust. Soc. Am. **146**(6), 4754–4773.

Zabalegui, P., De Miguel, G., Goya, J., Moya, I., Mendizabal, J., and Adín, I. (**2021**). "Residual based fault detection and exclusion methods applied to ultra-wideband navigation," Measurement **179**, 109350.